



Intuitive Machines' Odysseus lunar lander captured a wide field of view image of the moon's Schomberger crater on Thursday, at about 6 miles (10 kilometers) altitude and approximately 125 miles (200 kilometers) uprange from the spacecraft's intended landing site. Intuitive Machines

Landing Site Selection on the Moon: AI Role in Detection of Craters and Lunar Swirls

Ronald H. Freeman, PhD

Space Operations & Support Technical Committee, AIAA

Abstract

The lunar surface consists of a variety of geomorphological features like craters and lunar swirls. Detailed mapping of these features is important but tedious and time-consuming. Machine learning techniques address these issues by identifying the number of swirl units, then mapping them based on actual surficial spectral reflectance. Whereas previous missions were satisfied with a landing accuracy of a few kilometers, the polar region will require an accuracy within a few hundred meters. This paper aims to explore different image processing methods that employ convolutional neural networks (CNN) as a tool to improve accuracy in navigation and to pinpoint landing sites. One method to reduce landing and navigation errors is to employ a crater detector. LunaNet, visually detects craters in a camera image using a CNN and matches those detected craters to a database of catalogued lunar craters having known latitudes and longitudes. The output of LunaNet's CNN subsystem results in a prediction of image pixels discerning the crater rim according to the brightness. With an increased number of craters image-processed, a higher number of detected features reduces uncertainty of position estimates in terrain relative navigation. Specifically, the narrow ridges and small craters visible in LRO's narrow angle camera (NAC) images are also visible in the high-resolution digital elevation maps (DEM) when processed with a RANSAC algorithm. Therefore, selected landing site information is based on the local level of hazards, quantitatively defined in topological metrics of surface roughness, slope, presence of craters.

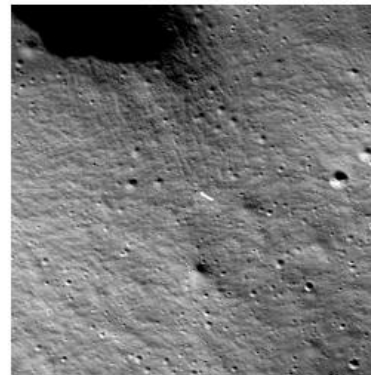
Keywords: Artificial Intelligence (AI), CNN, image processing, DEM, lunar landing site

Background

On Feb. 22, Intuitive Machines' Nova-C lander, called Odysseus, completed a seven-day journey to lunar orbit and landed near crater Malapert A in the South Pole region of the Moon at 6:24 p.m. EST. On Feb. 24, NASA's Lunar Reconnaissance Orbiter (LRO) spacecraft passed over the landing site at an altitude of about 56 miles (90 km) and photographed Odysseus. According to Tim Crain, chief technology officer, the IM-1 (Nova-C) landing location was identified about 1.5 kilometers from its intended landing site near Malapert A crater. Mark Robinson, principal investigator for the LRO camera, described Malapert A as a "degraded" crater about one kilometer across and the landing site with a relatively steep 12 degrees slope [Foust, J. (2024). Intuitive Machines expects early end to IM-1 lunar lander mission. Retrieved from www.spacenews.com].

NASA's Lunar Reconnaissance Orbiter captured this image of the Intuitive Machines' Nova-C lander, called Odysseus, on the Moon's surface on Feb. 24, 2024, at 1:57 p.m. EST. Odysseus landed at 80.13 degrees south latitude, 1.44 degrees east longitude, at an elevation of 8,461 feet (2,579 meters). The image is 3,192 feet (973 meters) wide, and lunar north is up. (LROC NAC frame M1463440322L). NASA/Goddard/Arizona State University

Nova-C lunar lander



1. Introduction

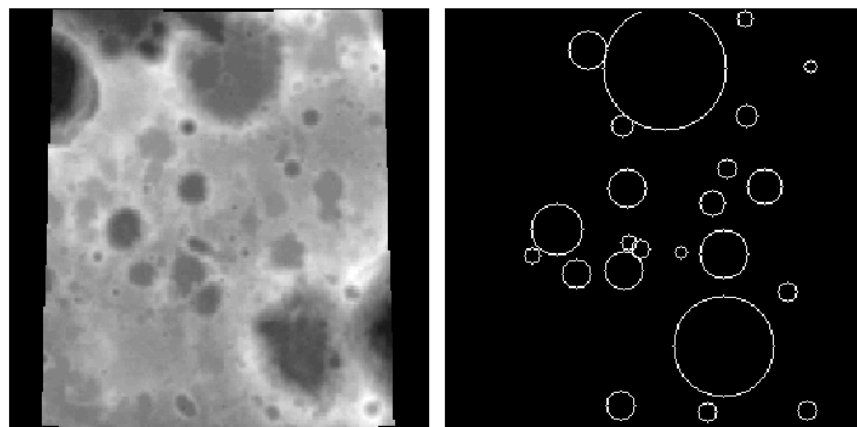
The lunar surface consists of a variety of geomorphological features like craters and lunar swirls. Detailed mapping of these features is important but tedious and time-consuming. For example, crater counting requires manual labeling of craters over a wide range of diameters. And, lunar swirls make the boundary between on- and off-swirls difficult to map with certainty. Machine learning techniques address these issues by identifying the number of swirl units, then mapping them based on actual surficial reflectance. Such metric includes I/F data of intensity changes due to the physical attributes of the surface, e.g. the roughness, single particle phase function, the single scattering albedo, and the compaction state of the optically active portion of the regolith [1]. Lunar mappings for both craters and swirls greatly benefit from ML- and AI-enabled automation with convolutional neural networks (i.e. tools from AI fields like computer vision [2]). Super-resolution approaches for remote mapping of the lunar surface employ multiple instruments onboard various lunar orbiters and rovers providing datasets of varying spatial resolutions. In most cases, very high resolution (targeted) datasets are not globally available. An AI-driven super resolution (SR) upscales a low-resolution image input to a higher resolution output for an intended landing site selection [3]. Since NASA's Commercial Lunar Payload Service (CLPS) landers will routinely deliver science and technology payloads to lunar surfaces of challenging conditions, a high degree of landing accuracy is necessarily important, particularly in the polar regions. Whereas previous missions were satisfied with a landing accuracy of kilometers [4], the polar region will require an accuracy within a few hundred meters. Also, very low descent rates will improve safety and probability of mission success. Most current powered descent phase guidance and control systems use two separate and independently optimized systems for guidance and control. The guidance system generates a trajectory that specifies the lander's target state as a function of time. The trajectory is then passed on to a control system that determines which thrusters to fire and at what thrust level. One approach to improve the accuracy in landing applies reinforcement learning (RL) algorithms. RL is used to learn guidance, navigation, and control (GNC) estimates of

thrust levels for each engine directly from commands [5]. An advantage of RL over traditional engineering GNC systems is its ability to adapt to unknown situations and circumstances that are difficult to foresee or cumbersome to account for manually. Therefore, as soon as uncertainty arises, challenges in autonomous navigation and control benefit from RL [6].

Proposed CLPS lunar payload deliveries will target the same small 1 x 5 km² region on the rim of Shackleton crater, located at the South Pole of the Moon [7]. The focus on accuracy suggests detecting craters and using them as landmarks since many have already been catalogued [8]. The difference between the expected crater location (based on estimated spacecraft pose) and the matched crater location generates a measurement of the error in the pose estimate. Spacecraft pose estimation is essential for maintaining or changing orientation in space [9]. An identifiable constellation of nearby craters signifies location of a crater. One method to reduce landing or navigation errors is to employ terrain relative navigation (TRN) by a crater detector (LunaNet) consisting of a “front end” and a “back end”. The “front end” uses sensors to observe the terrain around a vehicle and match those observations to known terrain. The “back end” uses matches to generate a state estimate of the vehicle. Vision-based TRN systems are especially attractive due to the small size, weight, and power requirements of space-rated cameras, as well as the rich data they provide.

Previous lunar landings relied mostly on inertial navigation methods, which time-integrate measurements from an inertial measurement unit (IMU). However, inertial navigation systems accumulate errors over time; and, past lunar landing errors have amounted up to several kilometers [10]. These errors pose a challenge because many future landing mission locations appear near hazardous terrains. LunaNet with a neural network, visually detects craters in a camera image and matches those detected craters to a database of catalogued lunar craters with known latitudes and longitudes. The inclusion of these measurements in a landing navigation system reduces estimation errors and enables increased precision with in-orbit navigation and that during landing [11].

Camera imagery varies due to time of day, electronic component heating, and model of camera and lens. The resultant image effects are difficult to predict with high degree of certainty, making it important that a crater detector be robust to such changes. Image processing-specific crater detectors have not demonstrated robustness to these variations, but machine learning’s strength for solving generalization problems allows crater detectors such as LunaNet to train for robustness to image variation. Convolutional neural networks (CNN) are tailored for image processing. For instance, CNNs are used for object recognition, image segmentation and classification [12]. Craters are a type of terrain landmark visible under a variety of lighting conditions. Current crater databases cover approximately 80% of the nearside of the Moon and significant portions of the farside. Crater segmentation maps are images with black backgrounds, and white rings corresponding to the pixel locations of crater rims in the DEM image, as shown in Figure 1.(b). Loss is an objective function, or the function that used to evaluate CNN success.



(a) Moon digital elevation map (DEM) input (b) Ground-truth craters in camera field of view. used to train DeepMoon.

Figure 1. Input image pairs used to train DeepMoon for crater detection from DEM.

Typically, loss measures error in CNN's classification. A lower loss denotes CNN output-produces an image matching the ground-truth target image. Ground-truth crater data is obtained from a combination of two human-generated lunar crater databases: the 5-20 km database of over 22,000 craters from [13] and the >20 km database of over 5,000 craters from [14], shown overlaid on the Moon in Figure 2.



Figure 2. Crater databases overlaid on the Moon. Craters from [13] shown in blue and craters from [14] shown in orange

2. The AI role in image processing of lunar craters

The use of AI for lunar landing selection is still at an early stage. Few works on AI exist in literature regarding image-based navigation. The AI system processes two kinds of inputs: images and measurements from an inertial measurement unit (IMU). The architecture comprising a CNN takes input streams of images and acts as a feature extractor. Images with different lighting and surface viewing conditions are used for training. The classical image processing (IP) algorithms provide a first estimate of the lander state (e.g., pose or altitude and position), which can be refined later by means of a navigation filter. The relative pose estimation of an inactive target by an active servicer spacecraft is a critical task in the design of space missions, due to its relevance for close-proximity operations [15]. The CNN is trained with an appropriate landing area dataset of synthetic images with different relative poses and under different illumination conditions. After the CNN-extraction of features, they are then passed on to a fully connected layer, which performs a regression and directly outputs the absolute camera pose [16].

LunaNet, visually detects craters in a camera image with a CNN) for image processing. These crater detections are matched to a database of catalogued lunar craters with known latitudes and longitudes [17]. The inclusion of these measurements in a spacecraft navigation system reduces the estimation error and enables increased-precision in-orbit navigation [18]. LunaNet inputs a raw camera image of the lunar surface taken from a nadir-facing camera. The camera image is then input to LunaNet's CNN subsystem that outputs a prediction image. The CNN's prediction of

image's pixels indicates the crater rim according to the brightness. The prediction image is then input to LunaNet's image processing subsystem which outputs a list of the locations and sizes in a pixel space of the craters.

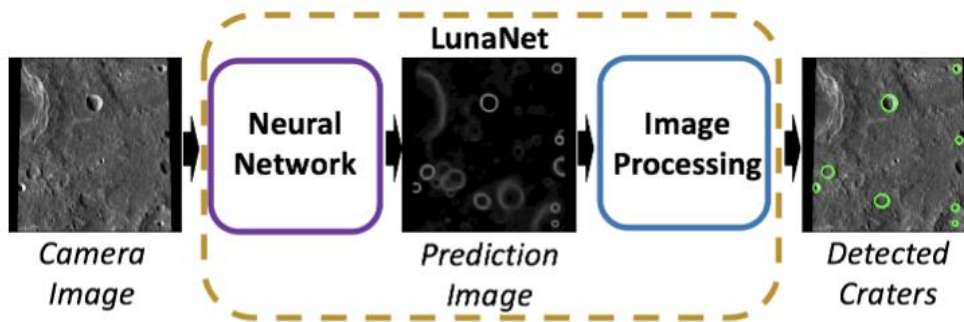


Figure 3. LunaNet system overview. System and subsystem labels are bolded, labels of inputs and outputs to those subsystems are italicized.

To detect craters, the input grayscale intensity image is thresholded for both bright and dark patches, which correspond to crater rims and shadows. Patch edges are detected (i.e. dark and bright pairs) and fitted with ellipses, representing crater rims. Due to the thresholding process, the crater detector identifies as a trinary edge detector. However, the trinary edge detector struggles to consistently detect the same craters, frame-to-frame in a trajectory. With significant sensitivity to image quality, brightness, and shadowing, precise tuning the trinary edge detector proves critical for performance. Precise tuning requires high levels of human input and detailed modeling and is only possible if the qualities of camera imagery and noise levels are known with high confidence prior to the mission. It is often difficult to predict these qualities, and they are not necessarily static during a mission. Recent work has demonstrated that significant improvements in robustness to lighting effects for automated crater detection are possible if more advanced technology avails in the fields of computer vision and deep learning [19].

The PyCDA is an open-source crater detection library composed of a detector, extractor, and classifier, which focuses on detecting new craters that have never been catalogued. PyCDA uses a downsized U-Net architecture to compute the per-pixel likelihoods of a crater rim from inputs of greyscale intensity images. The pixel prediction map is then fed to the extractor to generate a list of crater candidates, and a classifier CNN is applied to determine true craters. As a result, numerous craters have been detected and categorized to generate new labelled datasets for training and testing with deep learning (DL) algorithms [20]. DeepMoon network with a CNN architecture for robust crater detection on the lunar surface uses digital elevation maps (DEMs). The method relies on the developed DeepMoon network to identify craters in terms of their centroid and radii in order to output pixel-wise confidence maps of crater rims on the surface of a rocky body. DeepMoon [21] applies a CNN to detect craters from elevation data represented as overhead imagery and uses a U-net [22] architecture to perform pixel-wise classification of craters. After generating a prediction image of crater rim locations, DeepMoon uses template matching to obtain discrete crater detections from the prediction image. DeepMoon utilizes DEM imagery, which has significantly different micro-scale variation than camera imagery and is not affected by lighting effects such as glare and shadowing. Obtaining an accurate elevation map in-flight requires a space-rated range sensor such as radar or LiDAR, which is more expensive on average than a space-rated camera. Due to this, LunaNet uses camera images and thus must accommodate for shadows and other forms of visual noise.

The elevation images that DeepMoon was trained on are elevation maps of the Moon's surface obtained from the Lunar Reconnaissance Orbiter Camera (LROC) Wide Angle Camera (WAC), where a darker pixel corresponds to a depression and a lighter pixel corresponds to a raised area, as shown in Figure 1(a) [23]. The training images that DeepMoon inputs are sets of ground-truth classification data (known database craters) and DEM maps of corresponding areas on the Moon. This ground-truth crater data was obtained from a combination of two human-generated lunar crater databases: the 5-20 km database from [24] and the >20 km database from [25]. DeepMoon was trained for four epochs on 30,000 DEM images.

LunaNet combines CNN with image processing to detect craters in lunar surface imagery as captured by an onboard camera in real-time. The output of the neural network is a grayscale image with brighter pixels corresponding to predicted crater rims [26]. This output prediction is processed to identify likely craters that match against the databases of known craters in order to identify their true locations on the surface of the Moon [27]. The detected crater centers in the image and the known 3D locations of the craters can then be passed to a navigation filter that provides measurements needed to improve the estimates for spacecraft’s position and attitude and to correct for drift per the use of inertial sensors [28].

An estimated spacecraft location enables prediction of what craters should be in the camera field of view. To simplify simulations, spacecraft location estimates are set equal to true spacecraft locations. In order to test the crater matching performance, a search area is centered at the estimated spacecraft location which appears as wide as the camera field of view. The search area contains all the known, catalogued craters for that area, with their latitudes, longitudes, and radii. Such known craters are projected into the camera pixel space, assigning each known crater a size and location in pixels based on the location estimate. Detected craters are matched to known craters by means of nearest neighbor matched pairing in x, y pixel space, as well as in diameter in pixels. These pairs are then processed with random sample consensus (RANSAC) [29] to eliminate outlier pairs. A pair is determined to be an outlier if the translation vector between the detected crater and the known crater is sufficiently different from the translation vector of all inlier pairs, as seen in Figure 4.

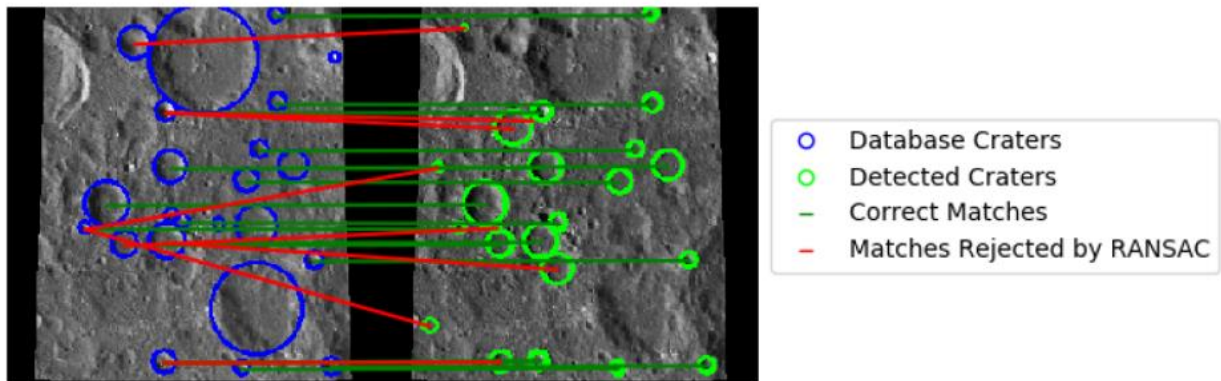


Fig. 4 Matching process of detected crater with database craters. Ground-truth set of craters that appear in the crater database for this test area in blue, craters detected by LunaNet in light green. Inlier pairs marked with dark green lines, outlier pairs marked with red lines.

This complete matching process is shown in Figure 5, with the final accepted matched craters shown in Figure 5(d). The difference between the matched crater location and the detected crater location generates a measurement of the error in the position estimate. This measurement can be used to improve the spacecraft position estimate by incorporating it into the navigation system, which includes an extended Kalman filter [30]. As the spacecraft moves around the Moon, repeated crater detections and matches can correct for the drift that is typical in inertial navigation systems.

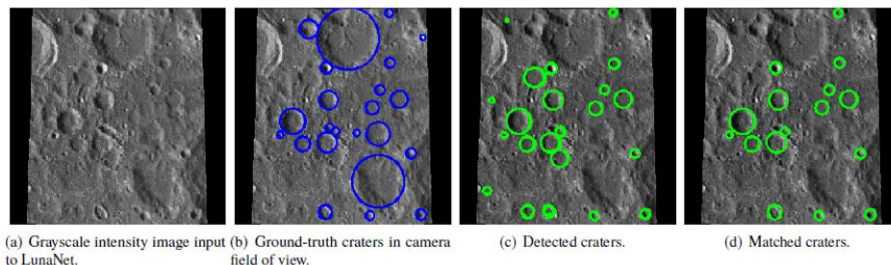


Fig. 5 Craters that were detected by LunaNet and matched to known craters in a representative LRO image with no noise added.

The higher the number of detected features in an image, the lower position estimate uncertainty in terrain relative navigation [31]. Detecting features with high accuracy benefits terrain relative navigation (TRN). Figure 6 shows the crater detection performance of the four crater detectors on the same image, an LRO image of a region near the lunar equator. These images show craters that were detected and successfully matched to known lunar craters. The threshold levels of the trinary edge detector were tuned to optimally detect craters in this LRO imagery. DeepMoon, PyCDA and the trinary edge detector all detect less than 50% the number of craters that LunaNet detects.

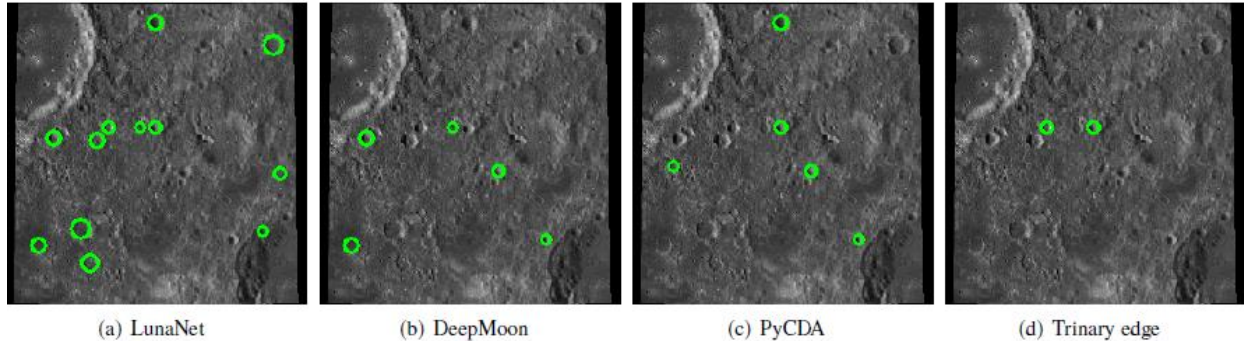


Fig. 6 Craters that were detected by different crater detectors and matched to known craters in a representative LRO image with no noise added.

LunaNet produces at least twice as many good crater detections on average as DeepMoon, PyCDA with another neural network crater detector, and the trinary edge detector, a thresholding-based crater detector. Since a higher number of features corresponds to better navigation performance in terrain relative navigation, LunaNet appears to be a promising option for crater-based visual terrain relative navigation.

3. The AI role in image processing of lunar swirls

Evidence of far-ranging dust transport in ‘swirls’ visible on the lunar surface refers to portions of lunar regolith that have bright, twisting streaks surrounded by darker areas. From spectroscopic analysis, the swirls appear to be deposits of lunar dust sometimes associated with regions of magnetic anomalies [32]. On examination, the swirls with respect to topography showed that the mean elevation of the bright portions of the swirls was statistically lower than the surrounding off-swirl regions. Hence, terrain-based swirls suggest origins of dust having traveled some distance before being deposited [33]. Other findings include associations with local crustal magnetic anomalies (Hood et al., 1979; Hood & Schubert, 1980); preliminary correlations between OH/H₂O spectral markers, suggesting mini-magnetospheres [34] capable of deflecting solar wind protons from the surface.

Using LROC NAC paired stereo images (e.g. two orbits O1 and O2 and two images L and R) per orbit results in a total of four images in pairs O1L and O1R, O2L and O2R) that are converted to I/F reflectance at a range of incidence angles. Maximum Likelihood Classification (MLC) algorithms classify and map portions of lunar swirls in Reiner Gamma and Mare Ingenii. Like the image classification method used when various types of land were identified from Earth-orbiting multispectral data (i.e. U.S. LANDSAT program), post-MLC images input into a predictive mathematical algorithm for training purposes to quickly classify scenes with many thousands to millions of pixels [35]. Algorithms confirm the number and location of these units and their interrelations. More importantly, the algorithms remove mapping subjectivity by using quantitative information. The data and the statistics generated from the maps also have value in future studies by placing limits for categorizing swirl units in different regions on the Moon [36].

In the supervised classification MLC, training areas for each swirl class (referred to as units) are digitized based on the representative albedo image providing the most inherent contrast per lowest incidence angle (Figures 7(a) and (b)). On-swirl areas typically have higher representative albedo, which generally defines many of the observed bright areas within a swirl. Off-swirls are generally areas with the lowest representative albedo and appear dark compared to on-swirl areas. Diffuse-swirls represent the transition from on- to off-swirls with an observed brightness intermediate between the two endmembers [37].

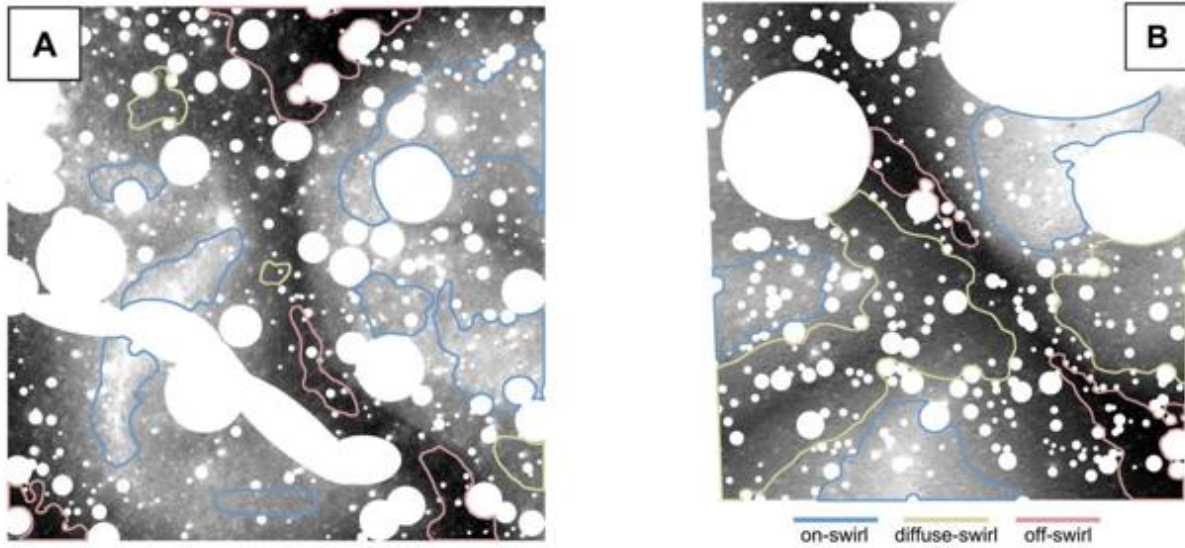


Figure 7. Locations of training areas in (A) Reiner Gamma and (B) Mare Ingenii for the three units of lunar swirls used in the MLC algorithm. On-swirl areas are outlined in blue, off-swirl areas in pink, and diffuse-swirl areas in tan.

For both study regions, the MLC classification maps generally match what is observed in the representative albedo images for all three units (Figures 8(a) and (b)). For Reiner Gamma, there is relatively even separation of reflectance ranges between on-, off-, and diffuse-swirl areas at each incidence angle using the MLC algorithm. Each unit has a distinct range of reflectance values, with overlap only at the extreme low and high ends of the range, typically the outermost 2%–3%. The separation further confirms the presence of a third principal swirl unit, the diffuse swirl [38]. Additionally, conversion of multi-spectral images to I/F reflectance at a range of incident angles applies MLC algorithms to classify and map lunar swirls that discern such spectral markers as crustal magnetic anomalies and H_2O/OH suggestive of mini-magnetospheres capable of deflecting solar wind protons from the regolith.

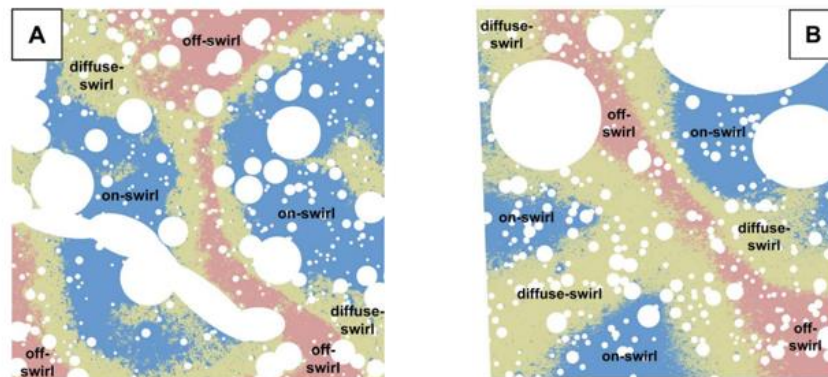


Figure 8. Classification maps using the MLC algorithm for the (A) Reiner Gamma and (B) Mare Ingenii study regions. Multiband albedo data including all three incidence angles were used in the algorithm for both study regions. On-swirl areas are shown in blue, off-swirl in pink, and diffuse-swirl in tan.

4. Lunar hazard avoidance-guided mission architectures

JPL's Autonomous Landing and Hazard Avoidance Technology (ALHAT) Project developed an integrated autonomous GNC hardware and software system capable of detecting and avoiding surface hazards. The Light Detection and Radar (LIDAR) sensor takes pictures of the shapes of an area rather than the color, essentially

providing an elevation map [39]. On the other hand, camera imaging incorporates CNNs for image processing to enable object recognition, image segmentation and classification. With an increased number of craters image-processed, a higher number of detected features reduces uncertainty of position estimates in terrain relative navigation. Specifically, the narrow ridges and small craters visible in the NAC image are also visible in the high-resolution DEM, while most of them are not apparent in the stereo DEM. Close to the rim of the crater in the eastern part of the image, boulders sized between 1 and 2 m are visible. A slope map indicates that for most of the region the slopes do not exceed values of 3-4 degrees, except for the walls of ridges and small craters. The depth to diameter (d/D) ratio and slope of the craters have been used to characterize craters namely, slope range and max slope along the wall which indicate a topographic roughness index (TRI) near a crater rim [40]. Such surface slope data are especially important for assessing the hazardousness of a potential landing site. Since many hazards are smaller than the highest resolution imagery available, developing and integrating automated hazard avoidance software as part of a spacecraft's guidance, navigation, and control software is critical to ensure safe landings on the Moon. The 2013 Chinese Chang'e-3 lunar lander mission successfully demonstrated that automated hazard avoidance software can be utilized to successfully achieve a safe powered descent and landing on the lunar surface [41]. At an altitude of 100 m above the lunar surface, the CE-3 spacecraft adjusted its thrust to enable it to enter a hovering stage. An optical imaging sensor was then utilized to detect impact craters or rocks on the surface that had diameters larger than 1 m. Landing camera images clearly showed that the spacecraft adjusted its position during this hovering stage, approximately 6 m in the north-south direction and 6 m in the east-west direction, to avoid obstacles [42].

Due to the long-time delays and the relatively low bandwidth characterizing radio communications from Earth, the exploration task must be entrusted to robotic platforms (e.g., landers and rovers) having advanced functionalities in terms of autonomous GNC capabilities and situational awareness [43]. For instance, an autonomous lander must guarantee a soft touchdown (which requires accurate knowledge of its navigation state [44] as well as the capability to execute complex control actions [45]), and select areas of high scientific interest, while ensuring safety simultaneously, by means of (1) adequate Hazard Detection and Avoidance (HDA) strategies and (2) low fuel consumption in accordance to proper guidance algorithms [46].

Information about the local level of hazards is quantitatively defined based on the local topological characteristics of the point cloud (i.e., surface roughness, slope, or presence of craters). The selection of the most convenient landing site is based on three different hazard metrics of slope, height and roughness, which are evaluated on a voxel-by-voxel basis. Specifically, the local values of these metrics for the point cloud elements are computed with respect to a Reference Ground Plane (RGP), which is derived by applying a RANSAC-based plane fitting algorithm to the entire DEM [44].

Reinforcement meta-learning along with hazard detection and avoidance are embedded into a single system in order to derive the optimal thrust command for a safe lunar pinpoint landing using sequences of images and radar altimeter data as inputs. The neural network used to recognize and label different areas of an image, consists of an encoder and a decoder. The encoder extracts information from the input image (Figure 9a) by applying a sequence of convolutional layers and reducing the image size. The decoder then upscales that information back to create a labeled image with the same size as the input [47].

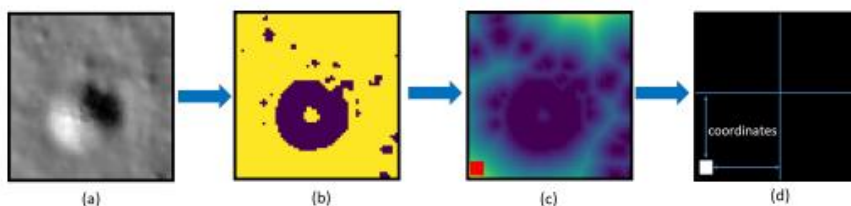


Figure 9. Hazard detection pipeline

The output of the network is a labeled image in which safe and unsafe areas are identified with different colors (Figure 9b). The algorithm then calculates the minimum distance from the closest hazardous pixel in the image matrix. The safest spot will then be the biggest among the minimum computed distances (Figure 9c). The position of this pixel in the focal plane (Figure 9d) is then passed onto the guidance algorithm.

Missions vary in location (nearside/farside/polar regions), duration (1 lunar day) missions and sample return capabilities. Broad-scale landing site requirements for missions preferentially select locations with (1) direct line-of-sight communications with Earth (i.e., on the nearside at nonpolar latitudes), (2) full solar illumination; (3) low slopes ($<10^\circ$), and (4) low density of surface hazards (boulders, impact craters, etc.). Mission capabilities specify static landers that operate for <1 lunar day although longer-term instruments, such as geophysical packages or retroreflectors, are also deployed [48]. The Lunar Orbital Platform-Gateway would potentially facilitate robotic missions on the lunar surface by acting as a communications relay and receiving samples returning from the farside of the Moon. Still, significant knowledge gaps exist and can only be filled by taking measurements of spacecraft landings.

5. Conclusion

The lunar surface consists of a variety of geomorphological features like craters and lunar swirls. Detailed mapping of these features is important but tedious and time-consuming. Machine learning techniques address these issues by identifying the number of swirl units, then mapping them based on actual surficial spectral reflectance. Whereas previous missions were satisfied with a landing accuracy of a few kilometers, the polar region will require an accuracy within a few hundred meters. This paper aims to explore different image processing methods that employ convolutional neural networks (CNN) as a tool to improve accuracy in navigation and to pinpoint landing sites. One method to reduce landing and navigation errors is to employ a crater detector. LunaNet, visually detects craters in a camera image using a CNN and matches those detected craters to a database of catalogued lunar craters having known latitudes and longitudes. The output of LunaNet's CNN subsystem results in a prediction of image pixels discerning the crater rim according to the brightness. With an increased number of craters image-processed, a higher number of detected features reduces uncertainty of position estimates in terrain relative navigation. Specifically, the narrow ridges and small craters visible in LRO's narrow angle camera (NAC) images are also visible in the high-resolution digital elevation maps (DEM) when processed with a RANSAC algorithm. Therefore, selected landing site information is based on the local level of hazards, quantitatively defined in topological metrics of surface roughness, slope, presence of craters.

References

- [1] Hicks, M. D., Buratti, B. J., Nettles, J., Staid, M., Sunshine, J., Pieters, C. M., ... & Boardman, J. (2011). A photometric function for analysis of lunar images in the visual and infrared based on Moon Mineralogy Mapper observations. *Journal of Geophysical Research: Planets*, 116(E6).
- [2] Bickel, V. T., Conway, S. J., Tesson, P. A., Manconi, A., Loew, S., & Mall, U. (2020). Deep learning-driven detection and mapping of rockfalls on mars. *IEEE Journal of Selected Topics in Applied Earth Observations and Remote Sensing*, 13, 2831-2841.
- [3] Bulyshev, A et al (2011). *A super-resolution algorithm for enhancement of FLASH LIDAR data*. Retrieved from www.ntrs.nasa.gov.
- [4] Phil Stooke (2016). *Lunar Farside Landing Plans*. Retrieved from www.planetary.org
- [5] Gaudet, B., Linares, R., & Furfaro, R. (2020). Deep reinforcement learning for six degree-of-freedom planetary landing. *Advances in Space Research*, 65(7), 1723-1741.
- [6] Izzo, D., Märtens, M., & Pan, B. (2019). A survey on artificial intelligence trends in spacecraft guidance dynamics and control. *Astrodynamics*, 3(4), 287-299.
- [7] Dahlstrom, E. & Pozza, M. (2022). New Risks of Future Lunar Landings. In: Pozza, M.A., Dennerley, J.A. (eds) *Risk Management in Outer Space Activities. Space Law and Policy*. Springer, Singapore.
- [8] Downes, L., Steiner, T. J., & How, J. P. (2020). Deep learning crater detection for lunar terrain relative navigation. In *AIAA SciTech 2020 Forum* (p. 1838).
- [9] Mo, L., Qi, N. & Zhao, Z. (2023). Spacecraft Pose Estimation Based on Different Camera Models, *Chin. J. Mech. Eng.* 36, 63.
- [10] Li, S., Jiang, X., & Tao, T. (2016). Guidance Summary and Assessment of the Chang'e-3 Powered Descent and Landing, *Journal of Spacecraft and Rockets*, 53, 258-277.
- [11] Singh, L., & Lim, S. (2008, August). On lunar on-orbit vision-based navigation: Terrain mapping, feature tracking driven EKF. In *AIAA Guidance, Navigation and Control Conference and Exhibit* (p. 6834). *Proceedings of the AIAA Guidance, Navigation and Control Conference*, Honolulu, Hawaii, 2008.
- [12] Silvestrini, S., & Lavagna, M. (2022). Deep learning and artificial neural networks for spacecraft dynamics, navigation, and control, *Drones*, 6(10), 270.
- [13] Barlow, N., Mest, S., Gibbs, V., & Kinser, R. (2012). Compilation of a Global GIS Crater Database for the Moon. In *AAS/Division for Planetary Sciences Meeting*, AAS/Division for Planetary Sciences Meeting Abstracts, page 311.05.
- [14] Cassinis, L., Fonod, R., & Gill, E. (2019). Review of the robustness and applicability of monocular pose estimation systems for relative navigation with an uncooperative spacecraft, *Progress in Aerospace Sciences*, 110.
- [15] Cassinis, L., Fonod, R., & Gill, E. (2019). Review of the robustness and applicability of monocular pose estimation systems for relative navigation with an uncooperative spacecraft, *Progress in Aerospace Sciences*, 110.
- [16] Silvestrini, S., & Lavagna, M. (2022). Deep learning and artificial neural networks for spacecraft dynamics, navigation and control, *Drones*, 6(10), 270.
- [17] Povilaitis, R., Robinson, M., van der Bogert, C. Hiesinger, H., Meyer, H., & Ostrach, L. (2018). Crater density differences: Exploring

- regional resurfacing, secondary crater populations, and crater saturation equilibrium on the moon, *Planetary and Space Science*, 162,41–51.
- [18] Downes, L. (2020). *Lunar orbiter state estimation using neural network-based crater detection* (Doctoral dissertation, Massachusetts Institute of Technology).
 - [19] Downes, L., Steiner, T., & How, J. (2020). Deep learning crater detection for lunar terrain relative navigation. In *AIAA SciTech 2020 Forum* (p. 1838).
 - [20] Silburt, A., Zhu, C., Ali-Dib, M., Menou, K., & Jackson, A. (2018). *DeepMoon: Convolutional neural network trainer to identify moon craters*, Astrophysics Source Code Library.
 - [21] Song, J., Aouf, N., & Honvault, C. (2022, May). Attention-based DeepMoon for Crater Detection. In *CEAS EuroGNC 2022*.
 - [22] Ronneberger, O., Fischer, P., & Brox, T. (2015). *U-Net: Convolutional Networks for Biomedical Image Segmentation*. arXiv:1505.04597.
 - [23] Scholten, F., Oberst, J., Matz, K.-D., Roatsch, T., Wählisch, M., Speyerer, E. & Robinson, M. (2012). Gld100: The near-global lunar 100 m raster DTM from LROC WAC stereo image data[J]. *Journal of Geophysical Research: Planets*117(E00H17).
 - [24] Povilaitis, R., Robinson, M., van der Bogert, C. Hiesinger, H., Meyer, H., & Ostrach, L. (2018). Crater density differences: Exploring regional resurfacing, secondary crater populations, and crater saturation equilibrium on the moon, *Planetary and Space Science*, 162,41–51.
 - [25] Head, J., Fassett, C., Kadish, S., Smith, D., Zuber, M., Neumann, G., & Mazarico, E. (2010). Global distribution of large lunar craters: Implications for resurfacing and impactor populations, *Science*, 329(5998). 1504–1507.
 - [26] Silburt, A., Zhu, C., Ali-Dib, M., Menou, K., and Jackson, A. (2018). DeepMoon: Convolutional neural network trainer to identify moon craters, *Astrophysics Source Code Library*.
 - [27] Povilaitis, R., Robinson, M., van der Bogert, C. Hiesinger, H., Meyer, H., & Ostrach, L. (2018). Crater density differences: Exploring regional resurfacing, secondary crater populations, and crater saturation equilibrium on the moon, *Planetary and Space Science*, 162,41–51.
 - [28] Head, J., Fassett, C., Kadish, S., Smith, D., Zuber, M., Neumann, G., & Mazarico, E. (2010). Global distribution of large lunar craters: Implications for resurfacing and impactor populations, *Science*, 329(5998). 1504–1507.
 - [29] Fischler, M. & Bolles, R. (1981). Random sample Consensus: A paradigm for model fitting with applications to image analysis and automated cartography, *Commun. ACM*, 24(6), 381–395.
 - [30] Mcgee, L., Schmidt, S., & Sc, S. (1985). Discovery of the Kalman Filter as a practical tool for aerospace and industry, *Tech. rep.*, National Aeronautics and Space Administration, Ames Research,
 - [31] Steiner, T., Brady, T., & Hoffman, J. (2015). Graph-based terrain relative navigation with optimal landmark database selection, *2015 IEEE Aerospace Conference*, 1–12.
 - [32] Domingue, D., Weirich, J., Chuang, F., Sickafoose, A., & Palmer, E. (2021). Topographic Correlations within lunar swirls in Mare Ingenii. *Geophysical Research Letters*, 49.
 - [33] Nardini, C. (2022). *Transient Lunar Phenomena, Outgassing Events, and the Lunar Gravity Field: Impacts to Sustained Human Presence on the Moon A master's thesis Submitted to the Faculty of* (Doctoral dissertation, American Public University System).
 - [34] Halekas, J., Delory, G., Lin, R., Stubbs, T., & Farrell, W. (2008). Lunar Prospector observations of the electrostatic potential of the lunar surface and its response to incident currents. *Journal of Geophysical Research*, 113, A09102.
 - [35] Chuang, F., Richardson, M., Weirich, J., Sickafoose, A., & Domingue, D. (2022). Mapping lunar swirls with machine learning: The application of unsupervised and supervised image classification algorithms in Reiner Gamma and Mare Ingenii. *The Planetary Science Journal*, 3(10), 231.
 - [36] Chuang, F., Richardson, M., Weirich, J., Sickafoose, A., & Domingue, D. (2022). Mapping lunar swirls with machine learning: The application of unsupervised and supervised image classification algorithms in Reiner Gamma and Mare Ingenii. *The Planetary Science Journal*, 3(10), 231.
 - [37] Chuang, F., Richardson, M., Weirich, J., Sickafoose, A., & Domingue, D. (2022). Mapping lunar swirls with machine learning: The application of unsupervised and supervised image classification algorithms in Reiner Gamma and Mare Ingenii. *The Planetary Science Journal*, 3(10), 231.
 - [38] Chuang, F., Richardson, M., Weirich, J., Sickafoose, A., & Domingue, D. (2022). Mapping lunar swirls with machine learning: The application of unsupervised and supervised image classification algorithms in Reiner Gamma and Mare Ingenii. *The Planetary Science Journal*, 3(10), 231.
 - [39] Zhang, H., Liang, J., Huang, X., Zhao, Y., Wang, L., Guan, Y., et al. (2014). Autonomous hazard avoidance control for Chang'E-3 soft landing. *Scientia, Sinica Technologica*, 44(6), 559–568.
 - [40] Agarwal, N., Haridas, A., Khanna, N., Srivastava, P., & Jain, V. (2019). Study of morphology and degradation of lunar craters using Chandrayaan-1 data. *Planetary and Space Science*, 167, 42-53].
 - [41] Liu, J.-J., Yan, W., Li, C. L., Tan, X., Ren, X., & Mu, L. (2014). Reconstructing the landing trajectory of the CE-3 lunar probe by using images from the landing camera. *Research in Astronomy and Astrophysics*, 14(12), 1530–1542.
 - [42] Wilcox, B. (1992). Robotic vehicles for planetary exploration, *Applied Intelligence*, 2 (2), 181-193.
 - [43] Xu, C., Wang, D., & Huang, X. (2016). Landmark-based autonomous navigation for pinpoint planetary landing, *Advances in Space Research*, 58 (11) 2313-2327
 - [44] Lee, U. & Mesbahi, M. (2017). Constrained autonomous precision landing via dual quaternions and model predictive control, *Journal of Guidance, Control, and Dynamics*, 40 (2), 292-308.
 - [45] Jiang, X., Li, S., & Tao, T. (2016). Innovative hazard detection and avoidance strategy for autonomous safe planetary landing, *Acta Astronautica*, 126, 66-76.
 - [46] Xiao, X., Cui, H., & Tian, Y. (2015). Robust plane fitting algorithm for landing hazard detection, *IEEE Transactions on Aerospace and Electronic Systems*, 51(4), 2864-2875.
 - [47] Scoroglio, A., D'Ambrosio, A., Ghilardi, L., Furfaro, R., Gaudet, B., Linares, R., & Curti, F. (2020, August). Safe Lunar landing via images: A Reinforcement Meta-Learning application to autonomous hazard avoidance and landing. In *Proceedings of the 2020 AAS/AIAA Astrodynamic Specialist Conference, Virtual* (pp. 9-12).
 - [48] Jawin, E. R., Valencia, S. N., Watkins, R. N., Crowell, J. M., Neal, C. R., & Schmidt, G. (2019). Lunar science for landed missions workshop findings report. *Earth and Space Science*, 6(1), 2-40].

